Phosphatidylinositol Phospholipids Modulate Hepatitis C Virus Core Protein Assembly on Lipid Membranes

Titas Mandal, Bastian Albrecht, Shorouk Abdelwahed, Jakob Ruickoldt, Peggy Jones, Petra Wendler and Salvatore Chiantia*

University of Potsdam, Institute of Biochemistry and Biology, Karl-Liebknecht-Str. 24-25, 14476 Potsdam, Germany

* Correspondence: chiantia@uni-potsdam.de

Abstract

Hepatitis C virus (HCV) genome codes for various proteins essential to its replication cycle. Among these, the core protein (HCC) forms the capsid via organised multimerization, thereby guiding viral assembly. This process depends on the dynamic localisation of HCC between the endoplasmic reticulum bilayer membrane and the lipid droplet monolayer. While past studies have examined the role of some HCC structural properties and other viral and host proteins in the assembly process, the contribution of lipid molecules was not thoroughly investigated yet. Since specific lipids are upregulated during HCV infection, it is reasonable that these molecules might play an important role for virus fitness and infection progression. In this study, we have addressed this topic and, specifically, how HCC-lipid interactions might impact HCC-HCC interactions. Using *in vitro* models and quantitative fluorescence microscopy techniques, we investigated HCC binding affinity to lipid membranes, multimerization and lateral diffusivity. Our results reveal the effect of HCC interactions with anionic phospholipids (PLs) on the binding to monolayers and bilayers. Furthermore, our analysis shows that PI(4)P enhances HCC multimerization and, therefore, might drive lateral assembly for capsid formation. These results not only provide insights into the lipid-driven regulation of HCV assembly and identify anionic PLs as potential modulators of the viral replications cycle, but also highlight a previously unrecognised role of PL composition in HCC-membrane interaction.

Significance

Hepatitis C virus (HCV) remains a major global health challenge and is associated with substantial mortality. In certain regions, HCV infection reaches epidemic proportions. Despite its prevalence, targeted and cost-effective therapeutic options remain limited, largely due to an incomplete understanding of the viral life cycle. A critical - yet poorly characterized - step in this cycle is the assembly of the HCV core (HCC) protein into the viral capsid, which is essential for replication. Here, we use quantitative fluorescence microscopy to investigate the role of specific lipid species in HCC assembly on model membranes. Our findings show that distinct lipid environments modulate HCC assembly and that HCC, in turn, induces measurable changes in the biophysical properties of the host membrane.

Introduction

Infection by Hepatitis C virus (HCV) is associated to severe liver disease and poses a serious global health challenge, due to the absence of vaccines and broadly accessible targeted medications (1–3). HCV is an enveloped virus with a 9.6 kb positive-sense RNA that codes for various viral proteins, including the Core protein (HCC) (4). HCC forms the structural subunits of the viral capsid, i.e. an icosahedral protective shell between the viral genome and the lipid envelope of the virus (5). Additionally, HCC plays fundamental roles in viral assembly (4–7), as well as hijacking of several host cellular pathways for sustaining the viral replication cycle (8–13).

HCV RNA translates into a polyprotein which produces ten individual viral proteins upon cleavage at specific sites by the host and viral peptidases (11). HCC is derived from the N-terminus of this polyprotein via the action of a host peptidase (11, 14, 15). The 191 amino acids (aa) long nascent HCC is targeted to the endoplasmic reticulum (ER) membrane owing to the presence of the C-terminal signal peptide (SP) domain (20 aa), which also acts as a bilayer transmembrane anchor (4, 16). Besides the SP, HCC includes two more domains: D1 and D2 (17). D1 is a larger (117 aa) hydrophilic domain enriched in basic amino acids. D2 is a shorter (54 aa) and more hydrophobic domain that consists of two amphipathic helices (H1 and H2) connected by a hydrophilic loop (HL) (16–18). Owing to the presence of the basic residues, D1 exhibits diverse interactions with the viral RNA (19–21) and, subsequently, promotes the formation of nucleocapsid (4, 22). Additionally, D1 promotes homotypic ionic interactions that form homo-multimers, necessary for capsid formation (6). The D2 domain, on the other hand, interacts with lipid membranes through its amphipathic character (16, 23). D2 additionally promotes HCC homo-dimer formation through a disulphide bond between the Cysteine residues (Cys128) of each protein (18). Such dimers play a notable role in the viral assembly by establishing the foundation for a stable nucleocapsid (5, 18, 24). As a part of the HCV replication cycle, HCC exhibits an organized dynamic partition between the ER bilayer membrane and lipid droplet (LD) monolayers (14–16, 25, 26). At the ER membrane, SP-peptidase-mediated cleavage of SP gives rise to the mature form of the HCC (171 aa) (16), which is subsequently escorted to the LD surface by host proteins (25, 27). The HCC-LD relationship is of paramount importance for the viral assembly process (15). For instance, HCC starts assembling into highly ordered multimers while on the surface of LDs, marking the first step of the viral assembly (15). Interestingly, arresting this step disrupts the viral life cycle (15) by inhibiting the transfer of HCC from the LD back to the ER (28–30). HCC multimer re-targeting to the ER membrane is actively mediated by other HCV proteins (4, 14, 26), and this translocation has been shown to assist in the late steps of the viral life cycle (31). These include synchronised packaging of the viral RNA with the HCC multimers and other viral proteins to form new viral particles (14, 26), which subsequently transit into the host secretory pathway (4, 22, 30, 32). Interestingly, HCC itself can form virions, independent of other viral proteins (15), indicating the fundamental role of this protein in virion production.

While (protein) host factors involved in HCC trafficking between ER and LDs were studied extensively (14–16, 25, 26), the influence of lipids in determining HCC localization and viral assembly are not well understood. Recent findings highlighted the role of neutral lipids such as triglycerides (TGs) in promoting D2 binding to artificial LDs (ALDs) or membrane bilayer models (i.e., giant unilamellar vesicles (GUVs)) (33). On the other hand, zwitterionic-phospholipids (PLs) such as phosphatidylcholine/ phosphatidylethanolamine were shown to hinder D2 interactions with both monolayers and bilayers (33). Otherwise, no detailed information is available regarding how specific PLs might affect HCC-lipid and HCC-HCC interactions. In this context, it is worth mentioning that, as a part of its host cellular pathway hijacking process, HCV upregulates the synthesis of certain anionic PLs such as phosphatidylinositol phosphates (PIPs) (which are in fact identified as "clinical hallmark" of HCV infection) (34–36). Despite their significant involvement in various stages of the HCV replication cycle (37), the possible contribution of anionic PLs in HCC trafficking and subsequent assembly is not known.

In this study, we clarify the role of anionic PLs in HCV assembly, using *in vitro* approaches. To this aim, we investigated the interaction of fluorescently labelled recombinant HCC (18) with model membranes, such as GUVs and ALDs representing PL bilayers (ER membrane) and LD monolayers, respectively (33, 38, 39). Specifically, we quantified HCC interactions with ALDs and GUVs in terms of binding affinity, multimerization, lateral dynamics and assembly using fluorescence fluctuation microscopy methods, namely line-scan fluorescence correlation spectroscopy (lsFCS) (40, 41). This method was successfully used in the past to study viral protein assembly, *in vivo* localisation and dynamics (41–43). By performing such a systematic analysis of the interactions between HCC and model membrane platforms composed of different PLs, we show that specific anionic PLs strongly influence HCC multimerization at the surface of LD, and, therefore, might play a fundamental role in the assembly of HCV.

Material and Methods

1. Materials

For the preparation of ALDs and GUVs, the detergent n-dodecyl β-D-maltoside (DDM) and the following lipids were purchased from Avanti Polar Lipids (Alabaster, AL, USA): 1,2-dioleoyl-sn-glycero-3-phosphocholine (DOPC), sphingomyelin (Milk, Bovine), 1,2-dioleoyl-sn-glycero-3-phospho-L-serine (DOPS), L-α-phosphatidylinositol-4-phosphate (Brain PI(4)P), L-α-phosphatidylinositol-4,5-bisphosphate (Brain PI(4,5)P2), 1-oleoyl-2-(6-((4,4-difluoro-1,3-dimethyl-5-(4-methoxyphenyl)-4-bora-3a,4a-diaza-s-indacene-2-propionyl)amino)hexanoyl)-sn-glycero-3-phosphocholine (TF-PC) and 1,2-distearoyl-sn-glycero-3-phosphoethanolamine-N-lissamine rhodamine B sulfonyl-ammonium salt (Rh-PE). Glycerine trioleate (Triolein) for the preparation of LDs, Alexa Fluor® 488 dye (AF488) and Alexa Fluor® 555 dye (AF555) for the calibration of excitation beam waist, and streptavidin for GUV chamber coating were purchased from Thermo Fisher Scientific (Waltham, MA, USA). Sucrose for electroformation was purchased from PanReac Applichem GmbH (Darmstadt, Germany). Tween®20, Tris-HCL, Tris base, magnesium chloride ($MgCl_2$), sodium chloride (NaCl), potassium chloride (KCl), urea, β-mercaptoethanol, Bovine serum albumin (BSA) for GUV chamber coating, disodium phosphate and monosodium phosphate for sodium phosphate buffer (NaP) preparation, and trifluoroacetic acid were purchased from Carl Roth GmbH (Karlsruhe, Germany). Skim milk for blocking buffer, PMSF, and DNase I were purchased from Sigma-Aldrich (St. Louis, Missouri, USA). EDTA-free protease inhibitor cocktail tablet was purchased from Roche Holding AG (Basel, Switzerland).

2. Vector expression and protein purification

The plasmid CMV-FLAG-Core-R (catalog no. 22480) for expressing HCC (genotype 1b), was purchased from Addgene (Watertown, MA, USA). A forward primer with Nde1 (TAACATATG**ATGAGCACGAATCCTAAACCTC**) and reverse primer with BamH1 (TTAGGATCC**CAGATTCCCTGTTGCATAGTTC**) cleavage site was designed to amplify a 507-bp nucleotide fragment corresponding to the 169 aa long HCC (18) from the purchased plasmid, using PCR. This amplified segment was then ligated into pET-15b vector (Novagene, catalog no. 70755, Burlington, MA, USA) and transformed into *E.coli* (BL21 AI strain) (Thermo Fisher Scientific, Waltham, MA, USA) for protein expression. N-terminal 6X-Histidine tagged HCC was expressed and purified following the available protocol by Boulant *et al*. (18) with slight modifications.

E.coli BL21 AI transformants were incubated in LB medium mixed with 100 µg/mL ampicillin at 37 °C (120 rpm) until the growth culture optical density (at 600 nm) reached ~0.7. Protein expression was induced using L-arabinose and IPTG at final concentrations of 0.2 % (w/v) and 1 mM, respectively, and allowed to grow for

132 a further three hours. Then, the bacterial cells were harvested by centrifugation at 4,248 x g. Following this,
133 the obtained pellet was resuspended in ice-cold Buffer A (25 mM Tris-HCL pH 7.5, 5 mM $MgCl_2$, 1 mM
134 PMSF, EDTA-free protease inhibitor cocktail tablet (1 tablet for 0.5 mL), and 100 µg/mL DNase I). Next, the
135 cells in the suspension were lysed using a French pressure cell press (Polytec, Germany) at 1200 psi and
136 centrifuged at 38,759 x g for one hour at 4° C. As expected (18), the expressed HCC was enriched in inclusion
137 bodies and, therefore, the pellet was further processed. The pellet was resuspended in Buffer B (20 mM Tris-
138 HCL pH 8, 500 mM NaCl, 6 M urea, 10 mM β-mercaptoethanol and 0.1 % (w/v) DDM) and sonicated for
139 homogenization. The homogenate was subjected to centrifugation. All centrifugation steps were performed
140 using Sorvall Lynx 4000 centrifuge (Thermo scientific, Waltham, MA, USA). Cell harvesting was performed
141 using a F12-6x500 LEX rotor (Thermo scientific, Waltham, MA, USA) and the remaining centrifugation steps
142 for protein separation were performed using a A27-8x50 rotor (Thermo scientific, Waltham, MA, USA).
143 The filtered supernatant was loaded over a Ni-NTA-agarose column (Qiagen, Germany) and purified using an
144 FPLC system (Biorad NGC chromatography system, Hercules, California, USA) following the manufacturer's
145 protocol. All purified fractions were screened by SDS-PAGE (15 % resolving gel) and Coomassie Blue
146 staining. The fractions consisting of HCC (~18 kDa) were isolated and further purified by reverse-phase HPLC
147 (Shimadzu, Japan) using a VYDAC 10 µm C8 column (250 x 4.6 mm) equipped with a 208TP Aquapore
148 guard cartridge (Avantor, Pennsylvania, USA). A linear gradient of acetonitrile in 10% trifluoroacetic acid was
149 used as the mobile phase. All fractions were monitored at 280 nm with an integrated UV-visible detector. The
150 main absorption peaks were screened by SDS-PAGE and silver staining. DDM was added (0.1 % (w/v) for 1
151 mg/mL protein) to the HCC containing fractions for protein stabilization. Finally, the HCC containing
152 fractions were lyophilized and stored at -20 °C until any further use. Unless mentioned, the lyophilized protein
153 fractions were resuspended in ice cold 20 mM NaP buffer (pH 7.4) when needed. For fluorescence microscopy
154 experiments, protein labelling was performed using the primary amine reactive dye Alexa Fluor® 488 (AF488)
155 following the manufacturer's protocol. In this regard, a degree of labelling (*DOL*) ~0.2 was reached, as
156 confirmed via optical spectroscopy measurements (data not shown).
157 Only a minor modification to the protocol was needed for the HCC mutant Δ68 (44) , which was purified from
158 the soluble fraction of the bacterial lysate using urea free buffer and labelled following the same protocol.
159
160
161 *3. PIP strip™ blotting*
162
163 PIP strips™ (Thermo Fisher Scientific, catalog no. P23751, Waltham, MA, USA) were used for screening the
164 PL binding preference of the purified HCC according to a published protocol (45). For blocking unspecific
165 interactions, each membrane was incubated in Buffer C (137 mM NaCl, 2.7 mM KCl, 19mM Tris base, 0.1 %
166 (v/v) Tween®20) + 1 % (w/v) skim milk (blocking buffer) for one hour at room temperature (RT).
167 Subsequently, the blocked strip was incubated overnight with 1 µg/mL unlabelled HCC in 20mM NaP buffer

168 at 4 °C. The incubated strip was then washed three times with Buffer C and subjected to one hour incubation
169 with mouse anti-HCV Core antibody (Thermo Fisher Scientific, catalog no. MA1-080, Waltham, MA, USA)
170 in blocking buffer (1/1000 dilution). The washing step was then repeated, followed by the addition of goat
171 anti-mouse alkaline phosphatase (AP) conjugated secondary antibody (Invitrogen, catalog no. 31320,
172 Waltham, MA, USA) (1/5000 dilution). After one hour incubation with the secondary antibody, the washing
173 step was repeated, and the membrane was treated with the AP substrate kit (BioRad, catalog no. 1706432,
174 Hercules, California, USA) for chromogenic detection of possible protein binding to the PL spots using the
175 manufacturer's protocol. Images of the developed membrane were acquired using an image scanner
176 (ImageScanner III, GE, Boston, MA, USA). Quantification of protein binding intensities was performed using
177 Fiji software (46).
178
179
180 *4. Preparation of ALDs*
181
182 ALDs were employed as *in vitro* lipid monolayer platforms for the quantitative investigation of HCC-lipid
183 interaction. ALDs were prepared using triolein as the oil phase according to an available protocol (47) with
184 slight modifications (39). Firstly, a PL solution mixed with 0.001 molar% (w/v) Rh-PE (or 0.005 molar% TF-
185 PC) in methanol was dried in a microcentrifuge tube under a nitrogen stream. The dried film was dispersed in
186 pre-warmed triolein (1/1000 mass ratio) and the mixture was extensively vortexed for 15 minutes and bath
187 sonicated for 30 minutes. Throughout the manuscript, triolein is referred to as "oil". The solution was then
188 added to 20 mM NaP buffer of pH 7.4 (1:10 v/v) and sonicated for ten seconds after short mixing, thus
189 obtaining a milky white oil-in-buffer emulsion which contained the ALDs. 75 μL of this ALD emulsion was
190 transferred to an observation chamber, which was diluted with an equal volume of the same buffer before
191 imaging. This procedure results in ALDs with monolayer mean molecular area (*MMA*) or area per PL values
192 roughly comparable to cellular or physiological LDs (i.e., ~80 $Å^2$/lipid, also referred to as *pMMA*) (48, 49),
193 as quantified via lsFCS (see below). To obtain three more different *MMA* values, the PL to oil mass ratio was
194 adjusted accordingly, e.g. 1/2000 PL/oil mass ratio for an increase in *MMA* as compared to *pMMA*, or 1/500
195 and 1/250 PL/oil mass ratios for a decrease in the *MMA* values. When needed, β-mercaptoethanol was mixed
196 to this solution to a 5 % (v/v) final concentration for experiments in reducing environment. Next, AF488-
197 labelled HCC was mixed to a final concentration of 200 nM and incubated for two hours. For Δ68, the final
198 concentration was 500 nM. In the case of experiments conducted to compare the multimerization of Δ68 and
199 HCC on the PL monolayer (i.e for experiments in which comparable binding to the ALD is needed for the two
200 proteins), the latter was added to a final concentration of ~20 nM. Following the incubation step, the sample
201 with the protein-ALD suspension was washed with 20 mM NaP to get rid of the unbound protein molecules.
202 It is worth mentioning that cellular LD monolayers contain small amounts (0.4-1 mol%) of anionic PLs (50,
203 51). However, to model the HCV infection condition (in which anionic PLs are upregulated) and observe

specifically the effect of specific anionic PLs on HCC binding, the model membranes studied in this work contained varying amounts of anionic PLs, up to 10 mol%.

5. *Preparation of GUVs*

GUVs as model of the ER bilayer (33) were used to investigate the binding behaviour of HCC to PLs. To highlight and compare the role of specific anionic PL, GUVs were prepared with the same PL compositions as ALDs by electroformation, using cylindrical Teflon chambers containing two platinum wires (52, 53) following an available protocol (39). PL solutions (2.5 mg/mL) were mixed with 0.005 molar% Rh-PE and 1 molar% biotinylated-PE. Following the electroformation, 100 µL of GUV suspension were transferred to an observation chamber, which was pre-treated with 100 µg/ml Streptavidin for 12 hours and then 10 % (w/v) BSA solution for 15 minutes. This suspension was further diluted with an equal volume of 40 mM NaP buffer and the GUVs were then allowed to settle down for 30 minutes, allowing the binding to the bottom of the plate. Next, AF488-labelled HCC was mixed to a final concentration of 200 nM and incubated for 2 hours. Finally, the GUVs were washed with 40 mM NaP to remove the unbound protein.

6. *Line-Scan fluorescence correlation spectroscopy*

Fluorescently labelled HCC binding, multimerization state and dynamics on ALDs and GUVs were quantified in terms of fluorescence intensity, brightness and diffusion coefficient ($D_{Protein}$), respectively, using lsFCS. Furthermore, the same approach was used to measure PL diffusion coefficient (D_{PL} or $D_{PL/TF\text{-}PC}$) and packing density (indicated by the *MMA*) in ALD monolayers labelled with 0.001 molar% Rh-PE (or 0.005 molar% TF-PC).

LsFCS was performed on GUVs and LDs based on previous protocols (39, 54). Briefly, membranes were scanned perpendicularly with a pixel dwell time of 0.67 µs (pixel size 0.08 µm) at resolution of 256 pixels (total scan time ~4 min). Large-scale (ca. > 1µm) PL or protein clusters on the membrane were avoided in order to scan a relatively homogenous region. Importantly, unless a cluster was present, scanning was always performed at the lower right side of the membrane (135°) of each ALD or GUV.

All images were acquired with a Zeiss LSM880 system (Carl Zeiss, Oberkochen, Germany) using a Plan-Apochromat 40x/1.2 Korr DIC M27 water immersion objective and a 32-channel gallium arsenide phosphide (GaAsP) detector array. AF488-labelled HCC bound to ALD or GUV surface were imaged using a 488 nm Argon laser (0.77 µW at the exit of the objective). Analogous experiments in samples without proteins were performed to determine *MMA* and D_{PL} in ALDs, using a 561 nm diode laser (1.97 µW). For measurements in the presence of HCC, D_{PL} was determined simultaneously with the protein measurement on the same ALD,

while for $D_{PL/TF\text{-}PC}$ determination, unlabelled HCC was used. For all measurements, the photobleaching and the background were kept below ca. 10 % / minute and 1% of the total initial intensity, respectively (54). In all cases, a commonly used bleaching correction and high-pass filters were applied (40).

In the case of ALD imaging, the significant difference in refractive index between the oil and aqueous phases results in imaging artifacts, such as enlargement of the point-spread function or unwanted reflections (causing e.g. the PL monolayers to appear as double lines, or a single abnormally broad line). Such distortions are stronger above the equatorial plane of ALDs partially adhering to the bottom glass coverslip. Imaging around the equatorial plane results in the best signal-to-noise ratio (48). Hence, all imaging was performed at this height. The validity of this approach was confirmed by comparing the PL packing density with that obtained using an alternative method described by Gandhi *et al*. (55), in which the ALDs are imaged at the south pole but they are not fixed to a coverslip (data not shown). Of note, such an approach could not be employed in general for this study, since the experiments described here require extensive washing to remove unbound proteins.

Prior to performing lsFCS, calibration of the excitation beam waist (w_0) was performed each day by measuring the fluorescence autocorrelation curve of 0.25 µM AF488 in 20 mM NaP to correct the laser alignment variation. This calibration procedure was also performed for the PL (Rh-PE) experiments, using a similar concentration of Alexa Fluor® 555 (Thermo Fisher Scientific, Waltham, MA, USA) (AF555) dye. Next, a mean of the diffusion times (τ_{Diff}) from three independent autocorrelation curves was used to calculate w_0 by applying the reported diffusion coefficient (D) of the fluorescent dyes (56, 57) following **Eq. 1**:

$$D = w_0^2 \,/\left(4 \cdot \tau_{Diff}\right) \qquad (1)$$

As an approximation, the ca. 2 % decrease in D due to the presence of the solute (58, 59) was neglected (39). Each data set was analysed as mentioned in previous work (39).

The effective illuminated area (A_{eff}) on the GUV or ALD was estimated as (40):

$$A_{eff} = \pi \cdot S \cdot w_0^2 \qquad (2)$$

wherein the structural parameter is denoted by S (derived as mentioned in previous work (39)).

The analysis of each measurement resulted in the number of particles (N) in the measured area, the integrated line intensity (I) and τ_{Diff} for the fluorophore (AF488 labelled HCC/ Rh-PE/ TF-PC). I was calculated as the time integral of the fluorescence signal in the immediate proximity of the membrane (60, 61) and expressed in Hz.

For the PL-only experiments, the total number of PL molecules in the illuminated area (N_{total}) was determined, which was used to calculate the PL *MMA* on the ALD surface (39):

$$MMA = A_{eff}/N_{total} \qquad (3)$$

For the measurements with AF488 labelled HCC, the measured I was normalized through i) the brightness value of AF488 (B_{dye}) obtained from daily calibration in solution (so to avoid errors caused by changes in laser power or optics alignment) and ii) the degree of labelling of the protein (so to correct for small sample-to-sample variations). In this regard, the typical DOL was ca. 0.2.
Protein brightness ($B_{Protein}$) was determined as (62):

$$B = I \,/\, N \qquad (4)$$

Hence, $B_{Protein}$ was expressed in Hz/molecule (Hz/mol) according to **Eq. 4**.

The I and $B_{Protein}$ values were converted into protein monomer concentration (mol/µm^2) and multimerization state, respectively. In this context, the number of protein monomers in the detection area was calculated by dividing the respective I value by the monomer brightness ($B_{monomer}$: in a rough approximation, the lowest $B_{Protein}$ value of all measurements). Next, the protomer concentration (i.e. protein concentration in units of equivalent monomer amounts) was obtained by dividing the number of protein molecules by the A_{eff}. Finally, the total number of bound proteins was obtained by dividing the labelled protein concentration by the DOL. Hence:

$$Protomer\ Concentration = \left({}^{I}/_{B_{monomer}}\right)/\left(A_{eff} \cdot DOL\right) \qquad (5)$$

Following this, the multimerization state from each brightness value was calculated based on the reported equation (62):

$$Multimerization\ state = 1 + \left[\left({}^{B_{Protein}}/_{B_{monomer}}\right) - 1\right]/DOL \qquad (6)$$

7. Transmission electron microscopy

ALDs (in Tris buffer) with or without HCC (200 nM) were negatively stained with uranyl acetate. Both samples were stained 2 hours after the preparation of the ALDs. 5 µL of sample were applied on a plain carbon

grid, incubated for 45 seconds (s) and subsequently washed four times in 5 µL droplets containing 2 % (w/V) uranyl acetate dissolved in water. Afterwards, the sample was incubated for 30 s and the excess solution removed by blotting. For each sample more than 100 transmission electron microscope (TEM) micrographs were collected on a Talos F200C microscope (Thermo Fisher scientific, Waltham, MA, USA) with a CETA camera at a magnification of 22,000x using an exposure time of 1 s.

8. Software

Statistical significance of differences between data sets were calculated using one-way ANOVA or two-sample t-test (significance level=0.05). All figures and statistical tests were made using Origin Pro 2024b (OriginLab Corporation, Northampton, MA, USA) (38, 39). Fluorescence microscopy images were processed using Fiji software. All data were analysed with MATLAB 2020b (The MathWorks, Natick, MA, USA) using already available codes (39). Primer designing was performed using Benchling (San Francisco, California, USA).

Results

1. Anionic PLs in LDs promote binding of HCC

HCV infection is associated to an increase in intracellular concentration of certain anionic PLs, such as PI(4)P and PI(4,5)P2 (8, 34, 36). However, it is not known whether these PLs play a role in HCC interactions with monolayers or bilayers. In order to understand the PL binding behaviour of HCC, we performed first a preliminary screening using immobilized PLs (i.e., PIP™ strips). PLs carrying different headgroups are presented on a nitrocellulose membrane and patterned as separate spots to test protein-PL interactions. Following this procedure, HCC binding was detected mostly within anionic PL spots with varying intensities, depending on the PL headgroup (**Figures 1A** and **S1**). The highest binding signal was observed for PI(4)P and PI(3)P, while that for the zwitterionic PL PC was among the weakest signals that could still be quantified (**Figure S1**). The results were reproducible, except for PI(3,4,5)P3, PI(3,4)P2, PI and PE which were, therefore, not further investigated. It is worth noting that the physical properties of PLs in this system, including their spatial organization and density, might differ from those of a PL monolayer on a water-oil interface and, therefore, must be accompanied by more in-depth investigation. For the following experiments, we thus focused on PI(4)P (as example of PIP with one phosphate group strongly interacting with HCC), PI(4,5)P2 (as example of PIP with two phosphate groups also interacting with HCC), PS (as an example of a non-PIP anionic PL still showing an interaction with HCC) and PC (as a negative control), as summarized in **Figure 1B**.

We proceeded to investigate HCC-lipid interactions directly in biophysical models of LDs by means of confocal microscopy and lsFCS. The latter measures the fluctuations in fluorescence emission from a spatially confined region of the membrane (see **Methods**) and calculates the labelled molecule mobility (in terms of D values), local abundance (in terms of the measured fluorescence signal I and the detected number of particles N) and multimerization state (in terms of brightness values) (40, 63). It is an advantage of this approach that brightness can be measured directly to determine the multimerization state, rather than relying on measurements of D that is, instead, only weakly dependent on protein mass (roughly, $D \propto \text{Mass}^{-1/3}$) (64).

First, we characterized protein-free ALDs to determine typical *MMA* values and the corresponding PL dynamics. By using multiple PL/oil mass ratios (see **Methods**), it is possible to cover an *MMA* range between ca. 40 and 120 Å²/PL (**Figure S2** and **Table S6**). It is worth noting that ALDs containing anionic PLs occasionally presented µm-scale lateral inhomogeneities (see e.g. **Figure S3A**) that were avoided during lsFCS measurements. PL mobility was quantified as a function of *MMA*, to confirm that the monolayer dynamics in our ALD model vary as expected (39, 65). Specifically, D_{PL} values increased from ~5 µm²/s to ~9 µm²/s (~6 µm²/s for PIPs) for increasing *MMA* values, as expected for unsaturated PLs at the oil-water interface (66) (**Figure S2E**). Also, we could identify the best PL/oil ratios needed for each PL composition to obtain *MMA* values either in the range 75-85 Å²/PL, i.e. *pMMA* (48, 49) or in the range 40-50 Å²/PL (i.e., an

358 arbitrarily chosen range, here defined as "low *MMA*"), as shown in **Table S6**. This estimation procedure is
359 needed later for samples containing proteins, in which the *MMA* of each ALD cannot be directly measured
360 (due to hindered PL dynamics and bleaching, see below). For example, to obtain *pMMA* samples, a PL/oil
361 mass ratio of 1:1000 is required for DOPC ALDs, while 1:500 is more suitable for DOPC + PI(4)P (9:1) ALDs.

362 Next, we analysed HCC binding by quantifying the fluorescence signal of AF488-labelled HCC bound to PL
363 monolayers formed at *pMMA*. For ALDs composed of the zwitterionic PL DOPC mixed with 10mol% of
364 different anionic PLs, increasing surface charge led in general to increasing protein binding (**Figure 1C**). Here,
365 we calculated that at pH 7.4, PI(4)P and PI(4,5)P2 possess a negative charge 2.94-fold and 4.2-fold higher
366 than DOPS, respectively (67). Of note, control experiments with fluorescent PL analogues suggest that the
367 different anionic PLs tested here partition into the monolayer in the expected amounts (**Figure S3**). A further
368 control experiment indicates that, after washing the unbound protein away, the unbinding kinetics are
369 significantly slower than the typical measuring time (**Figure S4**) and, therefore, the amount of bound protein
370 can be reliably measured at "quasi"-equilibrium and is independent from the small amount of residual protein
371 in solution.
372 Interestingly, the protein associates to the surface of ALDs even more efficiently if no PLs are present ("No
373 PL" condition in **Figure 1**). For ALDs prepared from pure DOPC, "low *MMA*" values (i.e. higher PL density)
374 are associated to a ca. 50% decrease in protein binding (cf. **Figures 1C** and **1D**, **Figure S5**), as expected from
375 previous reports suggesting that PLs forms a barrier that prevents the interaction between protein and LD
376 phase (33). Interestingly, we show that this effect was much less evident in the presence of anionic PLs i.e.,
377 ALDs containing 10 mol% DOPS (ca. 25% decrease in HCC binding) or PI(4)P (no decrease). Strikingly,
378 **Figure S5** shows that protein binding even increased at higher PL packing density in ALD monolayers
379 containing PI(4,5)P2, compared with the same ALDs at *pMMA*.
380 In order to clarify whether the observed interactions between HCC and anionic PLs are solely driven by non-
381 specific electrostatic interactions, we prepared ALDs with similar charge densities (i.e. DOPC monolayers
382 with 10mol% DOPS, 3.4mol% PI(4)P and 2.3mol% PI(4,5)P2). As shown in **Figure S6**, for p*MMA* samples
383 (**Figure S6A**), PI(4,5)P2 appears to bind the protein slightly more efficiently than PS. The effect is more
384 evident though in low *MMA* samples (**Figure S6B**), in which PI(4,5)P2 and, especially, PI(4)P exhibited a
385 significantly higher affinity to HCC, compared to DOPS, despite similar charge density.
386 Finally, **Figure 1E** and **S6E** show typical confocal microscopy images of the examined ALDs at *pMMA*, in
387 which the green channel indicates the AF488-labelled protein signal, and the red channel indicates the
388 fluorescent PL signal (0.001 mol% Rh-PE). In line with lsFCS quantification (**Figures 1C** and **S6A**), HCC
389 appears to bind efficiently to ALDs in the absence of PLs and much less when PLs form a monolayer at the
390 surface of the ALD (note the different colour scaling in the images). A similar trend and a general agreement
391 between confocal imaging and lsFCS is observed also at "low *MMA*" values/ high PL packing (**Figure S7**).

Microscopy imaging additionally indicates that the lateral distribution of PLs and HCC is not homogeneous in the presence of anionic PLs.

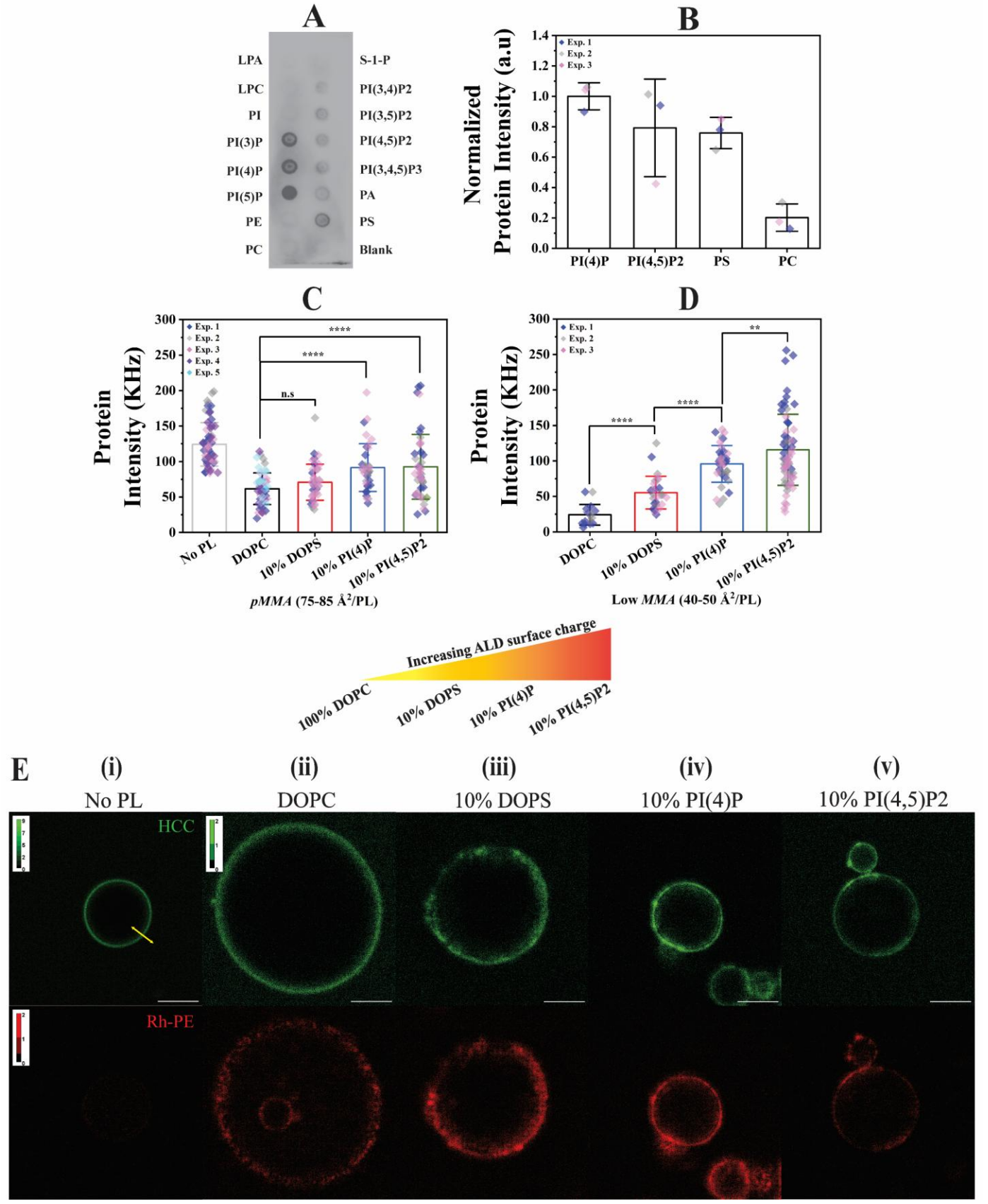

Figure 1: HCC binding to ALD monolayers depends on PL identity.
A shows a typical binding pattern of HCC to different lipids in a PIP™ strip detected using complementary antibodies. **B** shows the quantification of HCC binding intensity to each spot from three independent experiments for four selected

PLs. All data are normalized relative to PI(4)P. See **Table S1** for data points. **C** and **D** show the quantification of AF488-labelled HCC binding to ALDs performed via lsFCS and are represented as mean fluorescence intensity measured within the scanned region of the membrane (see Methods). **C** and **D** show the protein fluorescence intensity for ALD monolayers at *pMMA* and "low *MMA"* conditions, respectively. *MMA* values were not directly measured but rather estimated from protein-free ALDs prepared with the same PL/oil ratios (see **Table S6**). The ALDs are distinguished based on the interface PL composition: "No PL" refers to ALDs composed of only oil, "DOPC" to ALD monolayer composed of pure DOPC, "10% DOPS" to ALD monolayer composed of DOPC+DOPS (9:1 molar ratio), "10% PI(4)P" to ALD monolayer composed of DOPC+PI(4)P at 9:1 molar ratio and "10% PI(4,5)P2" to ALD monolayer composed of DOPC+PI(4,5)P2 at 9:1 molar ratio. All bars represent mean values with whiskers as the SD. Each point represents the result of one lsFCS measurement within one ALD. The points are pooled from at least two independent experiments denoted with individual colours. See **Tables S3**, **S4** and **S6** for details on statistics. Increasing surface charge trend of the ALDs as a function of different PL compositions is shown in form of a cartoon between panels **C**/**D** and **E**. For **C** and **D**, all statistical tests were performed via two-sample t-test at significance level 0.05 (**** $p<0.0001$, ** $p<0.01$, n.s: not significant). **E** shows representative fluorescence images of HCC-ALD interaction, in connection to the data in **C**. For each column, for the same samples shown in panel **C**, the green channel (top) represents AF488-labelled HCC, and the red channel (bottom) represents Rh-PE doped (0.001 molar%) ALDs. The yellow line in **(i)** depicts a typical scanning line used for lsFCS. The colour intensity range in the green channel for **(ii)**, **(iii)**, **(iv),** and **(v)** was rescaled with respect to that of **(i)** (lightest colour for pixels with 2 or more photons), for better visualization. Scale bar is 5 µm.

2. *PI(4)P promotes multimerization of HCC bound to LDs*

Further analysis of HCC-ALD interactions via lsFCS indicates that the average protein multimerization (quantified via molecular brightness, see **Methods**) does not strongly depend on the tested PL compositions, at least at *pMMA* (**Figures S8** and **S9A**). It is worth mentioning that fluctuation-based quantification of protein multimerization was performed in regions of the PL membrane that did not contain µm-scale clusters (see previous paragraph), as this method is based on the analysis of the (fast) diffusion of fluorescent objects much smaller than the size of the optical point spread function (ca. 300 nm) (40, 63). At higher PL packing or "low *MMA*", enhanced multimerization is observed for ALDs containing 10 mol% PI(4)P compared to e.g. 10 mol% DOPS or PI(4,5)P2 (**Figure S9B**) but, in general, a simple correlation between protein multimerization and *MMA* or PL identity is not evident over all the tested *MMA* values (**Figure S9C**). On the other hand, a clear trend is observed when plotting HCC multimerization as a function of local protein concentration (i.e., protein fluorescence intensity) (**Figure 2**). The observed molecular brightness values range from ~0.2 KHz/mol at low protein concentration to ~1 KHz/mol at the highest protein concentration measured, depending on PL composition. Considering that the protein labelling efficiency was ~0.2 dye molecules/protein and assuming that the lowest brightness we measured during this study (i.e. ~0.1 KHz/mol in GUVs, see below) corresponds to HCC monomers, it is possible to roughly estimate that HCC forms multimers with up to ca. 50 subunits in average, at concentrations ~1600 monomers/μm^2 (**Figure S10A**) in the presence of PI(4)P. For DOPS and PI(4,5)P2 this number was 20-35 subunits in average. Interestingly, such concentration-dependent multimerization is less evident for pure DOPC ALDs. Next, an empirical model (68) was fit to the data in **Figure S10A** and the results confirm that the multimerization is the most efficient in ALDs containing PI(4)P, while no significant difference can be observed for ALDs containing DOPC, DOPS or PI(4,5)P2 (**Table S6 v**).

Similarly to a previously published study (43), we aimed to test whether the protein-protein interactions observed here via lsFCS might be related to interactions which are relevant in the physiological context of virus capsid assembly. **Figure S11A** shows that, when bound to PI(4)P containing ALDs at similar concentrations as the wild-type protein, the assembly-incompetent HCC mutant Δ68 (44) exhibits a ca. 5- to 10-fold decreased brightness. Such brightness values are in the range of the lowest brightness values measured throughout this study (see below, for HCC bound to DOPC ALDs in reducing conditions, or HCC bound to PL bilayers) and might correspond to protein monomers or dimers. Also, for the samples in which we observed the most efficient protein multimerization (ALDs containing PI(4)P, as shown in **Figure S10A**), TEM imaging indicates the presence of regular structures with recurring spatial patterns with size between ca. 10 and 50 nm, that might correspond to the initial steps of viral capsid assembly (**Figure S12**).

Finally, we analysed the diffusive dynamics of HCC in ALDs under the investigated conditions (**Figures S10B** and **S13**). $D_{Protein}$ ranges from ~0.4 to ~1 μm²/s, with no strong correlation to protein concentration (**Figure S10B**), PL type (**Figures S13A** and **B**) or PL packing (**Figure S13C**).

In conclusion, the results so far indicate that negatively charged PLs (and, particularly, PIPs) promote HCC binding to ALDs. This effect is more easily observed if PLs are tightly packed within the monolayer. Furthermore, PI(4)P appears to enhance HCC concentration-dependent multimerization behaviour.

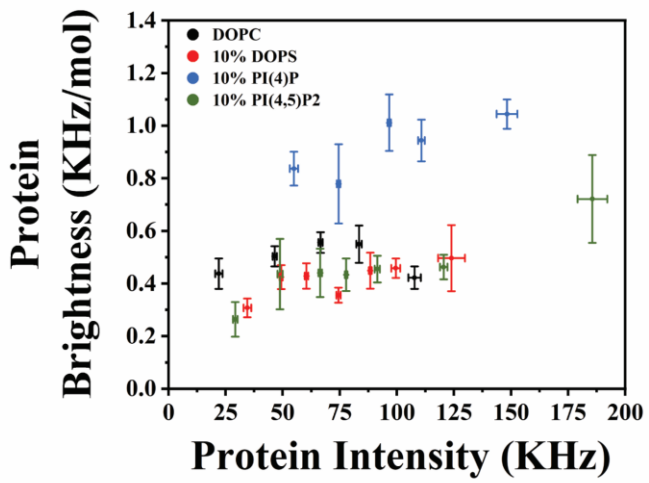

Figure 2: HCC brightness as a function of HCC concentration on ALDs.
HCC multimerization is quantified via the protein brightness obtained via lsFCS analysis. The figure shows the protein brightness values for each ALD composition plotted as a function of the corresponding protein fluorescence intensity values. Each colour indicates the parameters measured on ALD monolayers made of DOPC, DOPC+DOPS (9:1), DOPC+PI(4)P (9:1) and DOPC+PI(4,5)P2 (9:1). For better visualization, the data points were binned so that each point represents the mean value calculated from 9-43 points for DOPC LDs, 10-28 points for 10% DOPS mixed ALDs, 7-30 points for 10% PI(4)P mixed ALDs and 13-37 points for 10% PI(4,5)P2 mixed ALDs. The error bars represent the SEM calculated from the binning procedure. See **Table S7** for the details on the data points.

472 *3. Cysteine bridges are needed for effective HCC binding to ALDs*
473
474 It is known that the HCC forms dimers via inter-protein disulphide bonds (18). Such dimers have been shown
475 to be important for capsid stabilization, virus particle production (5, 24) and HCC-membrane interaction (5).
476 In comparison to non-reducing conditions (**Figures 1C** and **1E**), we found that the binding of HCC to ALDs,
477 irrespective of the monolayer PL composition, is significantly hindered in a reducing environment, as
478 evidenced by a ~5- to 10-fold decrease in the measured fluorescence intensity signal of the protein at the
479 surface of ALDs (**Figures 3A** and **B**). Interestingly, lsFCS analysis reported a strong decrease in protein-
480 protein interactions for DOPC ALDs (cf. **Figures S10A** and **3C**, **D**), as indicated by the low multimerization
481 values measured in this sample. The multimerization values observed for ALDs containing anionic PLs are,
482 on the other hand, comparable with those obtained before (**Figure S10A**, taking into account the lower
483 concentration of the bound protein), including the fact that the largest multimers are observed in the presence
484 of PI(4)P (e.g., between ca. 100 and 200 HCC protomers/μm^2). Finally, the decrease in protein binding to
485 ALDs does not appear to significantly modulate protein dynamics at the monolayer interface (cf. **Figures**
486 **S13A** and **S14**).

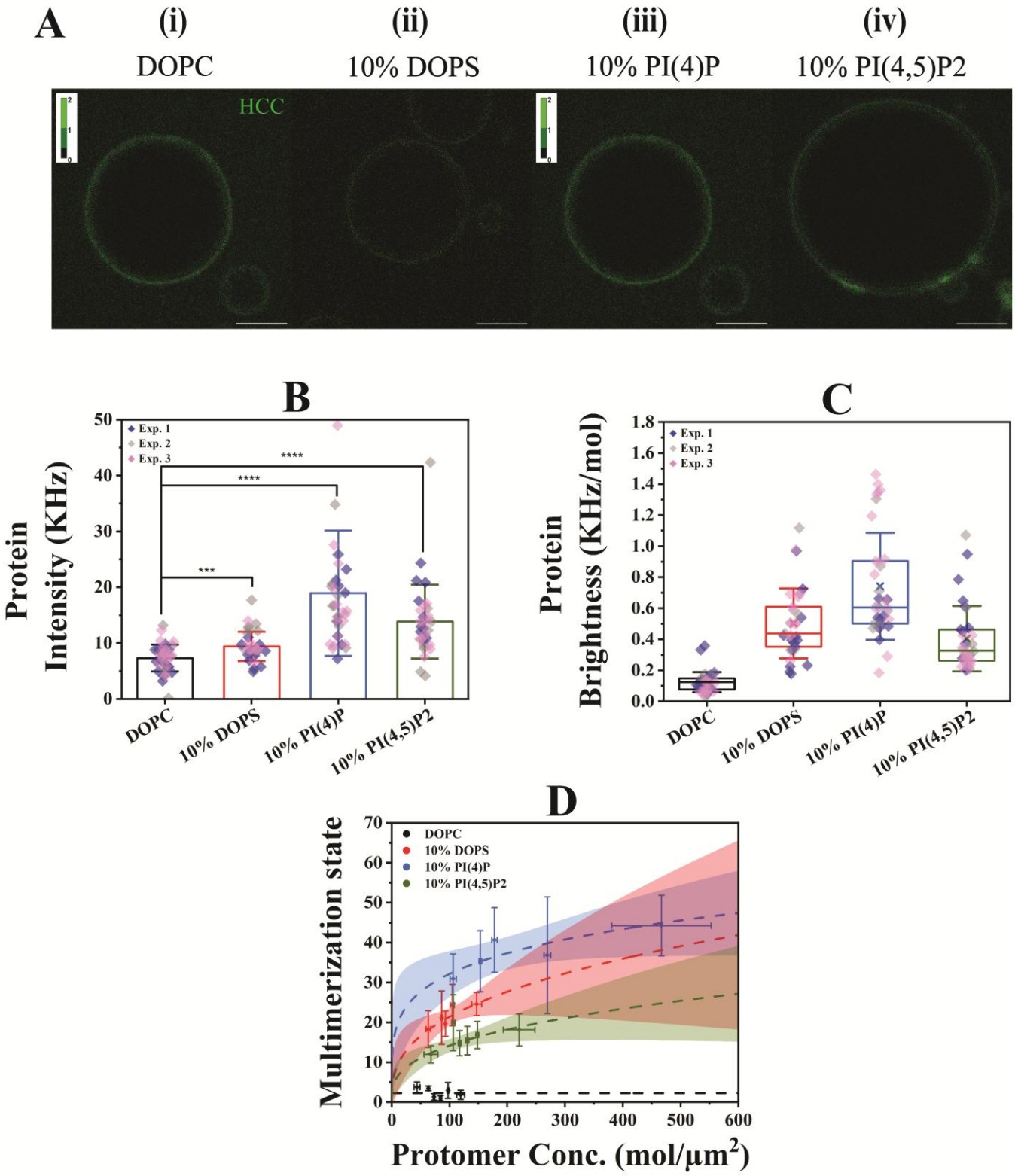

Figure 3: Decreased binding of HCC to ALD monolayers at *pMMA* in reducing environment.
Quantification of AF488 labelled HCC binding and multimerization on ALD monolayers at *pMMA* condition was performed in reducing environment via lsFCS analysis and is represented as fluorescent protein intensity and brightness, respectively. **A** shows typical fluorescence images of HCC bound to ALDs in reducing environment, **(i)** for ALDs made from DOPC, **(ii)** for ALDs made from DOPC+DOPS (9:1), **(iii)** for ALDs made from DOPC+PI(4)P (9:1) and **(iv)** for ALDs made from DOPC+PI(4,5)P2 (9:1). The colour intensity range in the green channel for **(ii)**, **(iii)**, **(iv),** and **(v)** was rescaled with respect to that of **Figure 1E (i)** (lightest colour for pixels with 2 or more photons), for better visualization. The scale bar is 5 µm. **B** shows the fluorescent protein intensity on ALDs derived from images exemplified in **A**, as bar graphs. All bars represent mean values with whiskers as the SD. All statistical tests were performed via two-sample t-test at significance level 0.05 (**** $p<0.0001$ and *** $p<0.001$). **C** shows the protein brightness values of HCC after

binding to the same set of ALDs, in the form of box plots. In all box plots, horizontal line is the median, 'x' marks the mean with first and third quartile as the boundaries and whiskers as SD. All data points were obtained from at least three independent experiments denoted with individual colours. **D** shows the protein multimerization state for each ALD composition plotted as a function of the corresponding protomer concentration values. Each colour indicates the parameters measured on ALD monolayers composed of DOPC, DOPC+DOPS (9:1), DOPC+PI(4)P (9:1), and DOPC+PI(4,5)P2 (9:1) respectively. For better visualization, the data points were binned so that each point represents the mean value calculated from 5-10 points for DOPC ALDs, 5-9 points for 10% DOPS mixed ALDs, 3-10 points for 10% PI(4)P mixed ALDs and 3-10 points for 10% PI(4,5)P2 mixed ALDs. Fitting was performed in the same way as for **Figure S10A**. 95% confidence interval range for each fit is shown by the respective colour bands. Protein concentration was obtained from protein intensity values and multimerization state was obtained from the corresponding brightness values using Eqs. 5 and 6 respectively. Error bars are SEM calculated from the binning procedure. The *a* value for 10% PI(4,5)P2 mixed ALDs is significantly lower than that for 10% DOPS and 10% PI(4)P mixed ALDs ($p<0.05$), as determined via one-way ANOVA at significance level 0.05. The *a* value difference between 10% DOPS and 10% PI(4)P mixed ALDs is not significant ($p>0.05$). Reducing environment was obtained through the addition of 5 % β-mercaptoethanol (v/v). See **Table S5** for the numerical values.

4. *Anionic PLs are necessary for the binding of HCC to PL bilayers*

In cells, removal of the SP from HCC results in its subsequent transfer from the ER bilayer to LD (25), which is the site of HCC multimerization - as a fundamental step of capsid assembly (15). Eventually, the HCC returns from the LD back to the ER bilayer (14, 26) and this re-targeting is crucial for efficient formation of virions (31). While it was reported that the D2 domain of HCC binds to bilayers exclusively in the presence of TG in the interleaflet region (33), the role of anionic PLs in this process has not been addressed yet. Therefore, we have investigated the interaction between HCC and GUVs containing different anionic PLs.

The binding of HCC to these bilayers is in general significantly (between one and two orders of magnitude) lower than to ALDs at *pMMA* (**Figures 4A** and **B,** cf. with **Figures 1E** and **C**). Interestingly, a fluorescence signal from the bound protein significantly above the background was observed exclusively in the presence of anionic PLs (**Figure 4A**). Probably due to the low concentration at the membrane, HCC does not significantly oligomerize, for all analysed compositions, as evidenced by multimerization states well below those measured for ALD-bound proteins (cf. **Figures S15** and **S10A**). LsFCS analysis also shows that diffusive dynamics of HCC on the GUV surface, i.e. $D_{Protein}$ values, are ~3 times faster than HCC bound to ALDs at *pMMA*, irrespective of the PL composition (**Figure 4C**). It is worth noting that HCC brightness (or multimerization) measurements and *D* quantification were not possible for GUVs containing exclusively DOPC, as the fluorescence signal from the bound protein was not sufficiently high for lsFCS analysis.

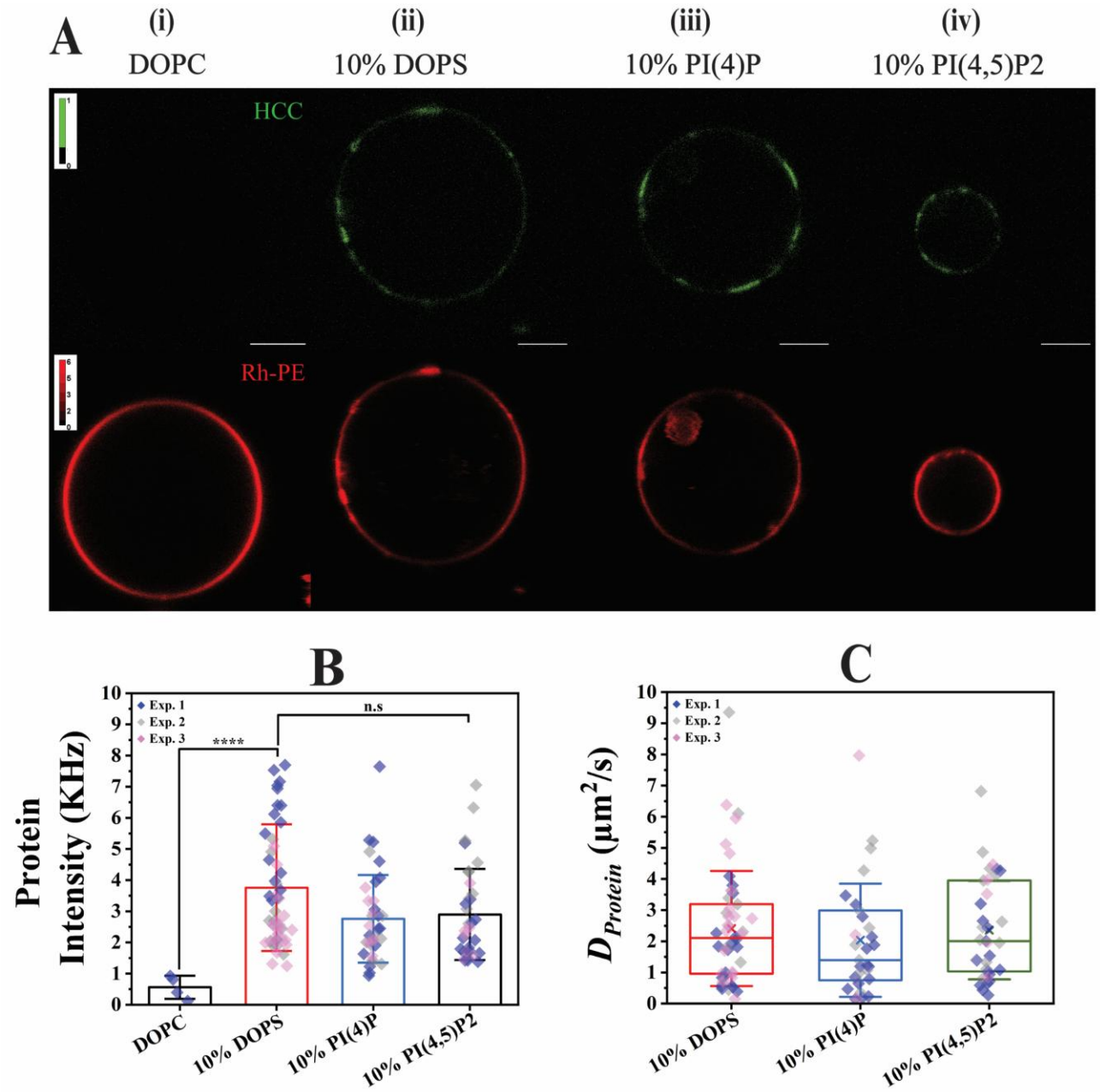

Figure 4: HCC binds to bilayer models only in the presence of anionic PLs.
Quantification of AF488 labelled HCC binding, multimerization and mobility via lsFCS analysis on GUVs composed of different PL species represented as protein intensity and diffusion coefficient ($D_{Protein}$). **A** shows typical fluorescence images of HCC bound to GUVs: **(i)** for GUVs made from DOPC, **(ii)** for GUVs made from DOPC+DOPS (9:1), **(iii)** for GUVs made from DOPC+PI(4)P (9:1) and **(iv)** for GUVs made from DOPC+PI(4,5)P2 (9:1). For each column, the green channel (top) shows the AF488 labelled HCC, and the red channel (bottom) shows Rh-PE labelled GUVs. The colour intensity range in the green channel was rescaled with respect to that of **Figure 1E (i)** (lightest colour for pixels with 1 or more photons), for better visualization. The red channel was also rescaled compared to **Figure 1E (i)** (lightest colour for pixels with 6 or more photons). Scale bar is 5 µm. **B** shows the fluorescent protein intensity on GUVs quantified from images exemplified in **A**, shown as bar graph. All bars represent mean values with whiskers as the SD. **C** shows the distribution of $D_{Protein}$ values from HCC binding to the same set of GUVs (except DOPC) in the form of box plots. GUVs of all PL compositions were labelled with 0.005 molar% Rh-PE for visualization purpose. In all box plots, the horizontal line is the median, 'x' marks the mean with first and third quartile as the boundaries and whiskers as SD. All data points were obtained from three independent experiments denoted with individual colours. In **B**, the differences between 10% DOPS, 10% PI(4)P and 10% PI(4,5)P2 mixed GUVs are statistically not significant. In **C**, mean $D_{Protein}$ values are not distinguishable. All statistical tests were performed via two-sample t-test at significance level 0.05 (**** $p<0.0001$ and n.s: not significant). See **Table S8** for the numerical values.

553 *5. HCC binding hinders PL dynamics in ALD monolayers*

554

555 In order to test the effect of protein binding on PL dynamics, we monitored the diffusion of the fluorescent PL
556 analogue Rh-PE (D_{PL}). The underlying assumption here is that the viscosity and the local membrane
557 environment sensed by the fluorescent PL are a good approximation of those sensed by the rest of the PLs
558 (39). Irrespective of the PL composition, D_{PL} in ALD monolayers at *pMMA* is strongly decreased (~10-fold)
559 following HCC binding (**Figure 5, Figure S16**). Interestingly, a decrease in lateral dynamics was also
560 observed for a structurally different fluorescent PL analogue TF-PC ($D_{PL/TF\text{-}PC}$), albeit by a much smaller
561 extent (i.e., ~3-fold decrease) (**Figure S16C**).

562

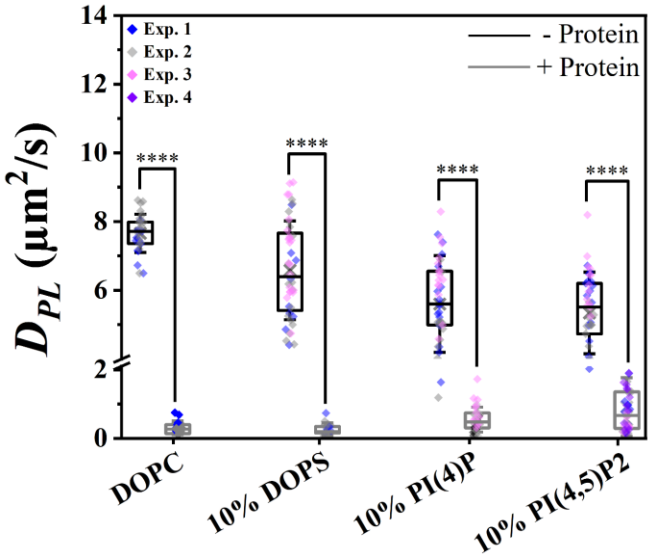

563

564 **Figure 5: ALD monolayer PL mobility decreases as a consequence of HCC binding.**
565 PL mobility in ALD monolayers composed of DOPC, DOPC+DOPS (9:1), DOPC+PI(4)P (9:1) and DOPC+PI(4,5)P2
566 (9:1) at *pMMA* (labelled with 0.001 molar% Rh-PE), represented as D_{PL} was analysed by lsFCS. All values are shown
567 in the form of box plots with the data points from two to three independent experiments. The data points for ALDs
568 without HCC are depicted in black boxes and those in the presence of HCC in grey boxes. In all box plots, the horizontal
569 line marks the median, 'x' marks the mean with first and third quartile as the boundaries and whiskers as SD. Statistically
570 different mean D_{PL} values are shown with ****. All statistical tests were performed via two-sample t-test at significance
571 level 0.05 (**** $p<0.0001$). See **Table S10** for the numerical values.

572

573

574 # Discussion

575 The binding of the HCC protein to the LD monolayer surface and subsequent return to the ER bilayer
576 membrane is a fundamental step of the HCV capsid assembly (4, 14, 15, 26). In this complex process, the role
577 of lipid molecules is not known yet, despite the evidence of significant upregulation of certain PL species in
578 the HCV infectious cycle (8, 34, 69). In this work, we aimed to investigate the possible function of specific
579 lipids in HCC-membrane interaction and subsequent assembly, as previous studies regarding HCC-LD
580 interaction did not address this aspect (16, 33, 70, 71). A more recent investigation by Ajjaji and colleagues
581 (33) highlighted the importance of triglycerides in the interaction between HCC and monolayers or bilayers.
582 However, these results were based on the investigation of ALD monolayers composed of only DOPC and

583 DOPE, thereby not addressing the possible effect of other (e.g. anionic) PLs, which are synthetized more
584 abundantly during HCV infection (36). In this context, it is worth noting that measuring the precise amount
585 of transient and precarious PLs such as PIPs might be quite complex (72). Furthermore, local concentration
586 of PIPs might be dramatically increased by preferential partitioning into lipid domains (37, 73–75). Therefore,
587 we have explored in this work a relatively large anionic PL concentration range (2-10 mol%), in general higher
588 that previous estimates of average relative concentrations (0.4-1 mol% (50, 51)), so to obtain a complete
589 picture of possible lipid-protein interactions.
590 Our experiments suggest that, irrespective of PL composition, the LD monolayer constitutes in general a
591 passive barrier to HCC-LD interaction, as HCC shows the highest binding to oil droplets devoid of PLs. In
592 analogy, HCC binding decreases dramatically, as more and more DOPC molecules are included in the
593 monolayer (**Figure S5**). A previous study showed a similar effect, albeit for a specific domain (i.e., D2) of this
594 protein (33). The oil-protein interaction seems therefore to dominate over possible PL-protein interactions
595 (**Figure 1**). As monolayer might have packing defects (76), HCC might use such defects to interact with the
596 oil phase (possibly via its amphipathic helix), rather than with (anionic) PLs (15, 33). Similar behaviour is
597 observed for several LD-binding proteins (76, 77). Nevertheless, even at *pMMA* conditions, HCC binding to
598 the ALD correlates with surface charge, assuming that each anionic PL contributes a negative charge
599 increasing in the order DOPS<PI(4)P<PI(4,5)P2. In agreement with this hypothesis, HCC interactions with
600 anionic PLs should be easier to detect if the interactions between protein and oil phase are hindered by a tighter
601 packing in the monolayer. Indeed, increasing monolayer PL density enhances HCC-LD binding in the presence
602 of e.g. PI(4,5)P2, opposite to what was observed for the zwitterionic DOPC (**Figure S5** and **1D**). Also, HCC
603 affinity towards anionic PLs does not appear to be driven exclusively by electrostatic interactions, as we
604 detected a stronger binding of the protein to PI(4)P-containing monolayers, among samples with comparable
605 negative surface charge (**Figure S6B)**. PI(4)P appears to play a specific role also in modulating protein-protein
606 interactions, as indicated by the enhanced concentration-dependant multimerization of HCC in ALDs
607 containing this PIP, compared to other anionic PLs possessing lower (i.e., DOPS) or higher (i.e., PI(4,5)P2)
608 negative charge (**Figure 2** and **S10A**). Of interest, in our ALD models, HCC forms multimers of up to ca. 50-
609 60 subunits in average (at a concentration of ca. 2500 mol/µm² and in the presence of PI(4)P), i.e. with a size
610 similar to what is expected for the forming HCV capsid (44, 78–80). The apparent role of PI(4)P in facilitating
611 capsid formation might relate to the observation that HCV infection is marked by high intracellular
612 concentrations of this PL (36).
613 The observation that anionic PLs in the LDs (and, specifically, PI(4)P) might increase HCC-HCC interactions
614 is further strengthened by experiments in reducing conditions (**Figure 3**). While inter-HCC cysteine bridges
615 have been proposed to stabilize the capsid and thereby control the viral assembly process (5, 24), our data
616 further suggest a role in promoting protein binding to the monolayer. Also, while protein multimerization is,
617 as expected, strongly decreased in reducing conditions for the case of DOPC monolayers, HCC multimers
618 remain instead apparently stable in the presence of anionic PLs, especially PI(4)P (**Figure 3D**). Once more,

these observations suggest that HCC-HCC and HCC-LD interactions are enhanced by anionic PLs, albeit not exclusively due to non-specific electrostatic interactions.

In the context of HCC multimerization on the surface of ALDs, as detected via fluorescence fluctuation analysis, it is important to determine whether the observed protein-protein interactions are related to non-specific random protein aggregation or, rather, to physiologically relevant interactions. The latter possibility is supported by our control experiments. First, we have shown that the multimerization detected via lsFCS for the assembly-incompetent mutant HCC Δ68 is, as expected, strongly decreased (44, 81) (**Figure S11**). Second, it would not be easy to reconciliate the hypothesis of random protein aggregation (e.g. at high protein density) with the observation of higher multimerization specifically in the presence of PI(4)P (instead of e.g. PI(4,5)P2). Third, TEM imaging indicates the presence of protein structures with regular spatial features, e.g. in the shape of crescents, that are compatible with the hypothesis of ordered protein-protein interactions, rather than non-specific protein aggregation (**Figure S12**). We propose therefore that the multimers reported in this work might represent indeed physiologically relevant HCC-HCC interactions and, possibly, correspond to the initial stages of HCV capsid formation. While fluorescence-based imaging approaches with higher spatial resolution (e.g. STED) (82, 83) might help further investigating this issue, it must be noted that the low label density (i.e. *DOL*) used in this work would represent a significant problem for such approaches (84). Also, a higher label density might hinder or alter the expected protein-protein interactions, as reported e.g. for the HIV-1 capsid (85).

Regarding the molecular mechanisms driving protein-LD interaction, the observations of HCC binding to tightly packed monolayers and the high affinity of the protein for the oil phase of ALD devoid of PLs are compatible with the hypothesis that the protein interacts with the oil phase and, concurrently, to anionic PLs via specific electrostatic interactions. Also, the presence of direct, albeit weak, interactions between HCC and anionic PLs is confirmed by our experiments on model bilayers (**Figure 4)**. While triglycerides were shown to promote the binding of HCC to bilayers (33) (e.g. to the ER), we demonstrate here that the presence of small concentrations of anionic PLs is also sufficient to obtain a protein binding significantly higher than that observed in the presence of only zwitterionic PLs. Of note, HCC binding to bilayers remains nevertheless much lower than the one observed in the case of monolayers and, as expected, is associated to much weaker protein-protein interactions (due to lower local concentration on the membrane, see **Figure S15**). In this context, the much slower diffusive dynamics of HCC on monolayers compared to bilayers (cf. **Figure 4C** and **S13**) suggest that the protein binds only superficially to bilayers (i.e. to PL headgroups (39)). On the other hand, in monolayers, the protein might at least partially insert into the highly viscous oil-phase (33), thus slowing down its lateral diffusion.

The last part of our work focuses on the effect of protein binding on the properties of the PLs in the LD monolayer. Since we hypothesize that direct interactions might exist between anionic PLs and oligomers (or large multimers) of HCC, it is reasonable to expect that protein binding might affect the lateral diffusion of PLs in the membrane (86, 87). Furthermore, it was also reported that PL dynamics is affected by the insertion

of proteins into a monolayer or a membrane leaflet (87, 88). Accordingly, our results indicate a strong decrease in diffusive dynamics of a fluorescent PL probe (Rh-PE) after binding of HCC to the monolayer (**Figure 5**). Interestingly, the diffusion of a structurally different fluorescent PL (TF-PC) also decreases in the presence of a protein, but by a much smaller extent. Assuming that Rh-PE carries a negative charge at pH 7.4, while TF-PC remains neutral, the latter PL probe would report a general decrease in diffusive dynamics for all PLs in the monolayer (due e.g. to the insertion of the protein and the consequent increase in PL packing). On the other hand, the dramatic decrease of diffusive dynamics of Rh-PE might instead indicate that this anionic fluorescent PL (similarly to the other anionic PLs in the monolayer) binds to the bulky protein multimers and, as a consequence, diffuses at a much slower rate.

Conclusions

This work shows that anionic PLs, specifically PI(4)P, affect HCC multimerization on monolayers (as models of LDs), probably by modulating the local concentration of the protein. In this scenario, HCC can be hypothesized to interact with the neutral lipid phase of LD and concurrently, although less strongly, with the polar heads of anionic PLs. Such significant involvement of anionic PLs could be one of the reasons why these are more abundant during HCV infection (8, 34, 36). Furthermore, we show that, through insertion in the monolayer or by recruiting specific PLs, HCC has the potential to alter the biophysical properties of LD monolayers. While the simplified model system used in this work was necessary to pinpoint specific lipid-protein interactions, future studies should investigate the role of more complex, physiologically relevant PL compositions and, most importantly, the role of other host or viral proteins.

Author contributions

TM and SC conceived the research. TM, BA, SA, JR, PW and PJ performed the experiments and analysed the results. SC wrote the MATLAB codes for data analysis. TM and SC wrote the manuscript.

Acknowledgements

TM would like to thank the Postgraduate Scholarship Committee of the University of Potsdam, Germany for his Doctoral dissertation completion scholarship and funding this project. We thank the members of the group, especially Dr. Anja Thalhammer for their valuable comments and discussions. Additionally, TM would like to

thank Nadine Brandt for her help in preparing the supplemental tables and Melanie Anding for help with the TEM experiments.

Declaration of interests

The authors declare no competing interests.

Declaration of generative AI and AI-assisted technologies in the writing process

During the preparation of this work, TM used GPT.UP (OpenAI GPT-40) in order to improve the readability and language of the abstract and significance. After using this tool/service, the authors reviewed and edited the content as needed and take full responsibility for the content of the publication.

References

1. World Health Organization, HCV, 2024. 12 June 2024. https://www.who.int/news-room/fact- 856 sheets/detail/hepatitis-c.
2. National Health Service, 2022, Hepatitis.12 June 2024. https://www.nhs.uk/conditions/hepatitis-c/.
3. Adugna, A. 2023. Therapeutic strategies and promising vaccine for hepatitis C virus infection. *Immun Inflamm Dis*. 11.
4. Gawlik, K., and P.A. Gallay. 2014. HCV core protein and virus assembly: what we know without structures. *Immunol Res*. 60:1–10.
5. Kushima, Y., T. Wakita, and M. Hijikata. 2010. A Disulfide-Bonded Dimer of the Core Protein of Hepatitis C Virus Is Important for Virus-Like Particle Production. *J Virol*. 84:9118–9127.
6. Matsumoto, M., S.B. Hwang, K.-S. Jeng, N. Zhu, and M.M.C. Lai. 1996. Homotypic Interaction and Multimerization of Hepatitis C Virus Core Protein. .
7. Ai, L.-S., Y.-W. Lee, and S.S.-L. Chen. 2009. Characterization of Hepatitis C Virus Core Protein Multimerization and Membrane Envelopment: Revelation of a Cascade of Core-Membrane Interactions. *J Virol*. 83:9923–9939.
8. Syed, G.H., Y. Amako, and A. Siddiqui. 2010. Hepatitis C virus hijacks host lipid metabolism. *Trends in Endocrinology & Metabolism*. 21:33–40.

9. Thaker, S.K., J. Ch'ng, and H.R. Christofk. 2019. Viral hijacking of cellular metabolism. *BMC Biol*. 17:59.

10. Mani, H., J.-H. Yen, H.-J. Hsu, C.-C. Chang, and J.-W. Liou. 2022. Hepatitis C virus core protein: Not just a nucleocapsid building block, but an immunity and inflammation modulator. *Tzu Chi Med J*. 34:139.

11. Ray, R.B., and R. Ray. 2001. Hepatitis C virus core protein: intriguing properties and functional relevance. *FEMS Microbiol Lett*. 202:149–156.

12. Jackel-Cram, C., L.A. Babiuk, and Q. Liu. 2007. Up-regulation of fatty acid synthase promoter by hepatitis C virus core protein: Genotype-3a core has a stronger effect than genotype-1b core. *J Hepatol*. 46:999–1008.

13. Paracha, U.Z., K. Fatima, M. Alqahtani, A. Chaudhary, A. Abuzenadah, G. Damanhouri, and I. Qadri. 2013. Oxidative stress and hepatitis C virus. *Virol J*. 10:251.

14. Shavinskaya, A., S. Boulant, F. Penin, J. McLauchlan, and R. Bartenschlager. 2007. The Lipid Droplet Binding Domain of Hepatitis C Virus Core Protein Is a Major Determinant for Efficient Virus Assembly. *Journal of Biological Chemistry*. 282:37158–37169.

15. Vieyres, G., and T. Pietschmann. 2019. HCV Pit Stop at the Lipid Droplet: Refuel Lipids and Put on a Lipoprotein Coat before Exit. *Cells*. 8:233.

16. Boulant, S., R. Montserret, R.G. Hope, M. Ratinier, P. Targett-Adams, J.P. Lavergne, F. Penin, and J. McLauchlan. 2006. Structural determinants that target the hepatitis C virus core protein to lipid droplets. *Journal of Biological Chemistry*. 281:22236–22247.

17. Izumida, K., and E. Morita. 2024. The roles of HCV core protein and its binding host factor in virus assembly and release. *Frontiers in Virology*. 4.

18. Boulant, S., C. Vanbelle, C. Ebel, F. Penin, and J.-P. Lavergne. 2005. Hepatitis C Virus Core Protein Is a Dimeric Alpha-Helical Protein Exhibiting Membrane Protein Features. *J Virol*. 79:11353–11365.

19. Sharma, K.K., H. de Rocquigny, J.L. Darlix, J.-P. Lavergne, F. Pénin, J.-M. Lessinger, and Y. Mély. 2012. Analysis of the RNA chaperoning activity of the hepatitis C virus core protein on the conserved 3′X region of the viral genome. *Nucleic Acids Res*. 40:2540–2553.

20. Ivanyi-Nagy, R., I. Kanevsky, C. Gabus, J.-P. Lavergne, D. Ficheux, F. Penin, P. Fosse, and J.-L. Darlix. 2006. Analysis of hepatitis C virus RNA dimerization and core-RNA interactions. *Nucleic Acids Res*. 34:2618–2633.

21. Cristofari, G. 2004. The hepatitis C virus Core protein is a potent nucleic acid chaperone that directs dimerization of the viral (+) strand RNA in vitro. *Nucleic Acids Res*. 32:2623–2631.

22. Kunkel, M., M. Lorinczi, R. Rijnbrand, S.M. Lemon, and S.J. Watowich. 2001. Self-Assembly of Nucleocapsid-Like Particles from Recombinant Hepatitis C Virus Core Protein. *J Virol*. 75:2119–2129.

23. Pérez-Berná, A.J., A.S. Veiga, M.A.R.B. Castanho, and J. Villalaín. 2008. Hepatitis C virus core protein binding to lipid membranes: The role of domains 1 and 2. *J Viral Hepat*. 15:346–356.

24. Murray, C.L., C.T. Jones, J. Tassello, and C.M. Rice. 2007. Alanine Scanning of the Hepatitis C Virus Core Protein Reveals Numerous Residues Essential for Production of Infectious Virus. *J Virol*. 81:10220–10231.

759 25. Herker, E., C. Harris, C. Hernandez, A. Carpentier, K. Kaehlcke, A.R. Rosenberg, R. V Farese, and
760 M. Ott. 2010. Efficient hepatitis C virus particle formation requires diacylglycerol acyltransferase-1.
761 *Nat Med*. 16:1295–1298.

762 26. Boson, B., O. Granio, R. Bartenschlager, and F.-L. Cosset. 2011. A Concerted Action of Hepatitis C
763 Virus P7 and Nonstructural Protein 2 Regulates Core Localization at the Endoplasmic Reticulum and
764 Virus Assembly. *PLoS Pathog*. 7:e1002144.

765 27. Menzel, N., W. Fischl, K. Hueging, D. Bankwitz, A. Frentzen, S. Haid, J. Gentzsch, L. Kaderali, R.
766 Bartenschlager, and T. Pietschmann. 2012. MAP-Kinase Regulated Cytosolic Phospholipase A2
767 Activity Is Essential for Production of Infectious Hepatitis C Virus Particles. *PLoS Pathog*.
768 8:e1002829.

769 28. Gentzsch, J., C. Brohm, E. Steinmann, M. Friesland, N. Menzel, G. Vieyres, P.M. Perin, A. Frentzen,
770 L. Kaderali, and T. Pietschmann. 2013. Hepatitis C Virus p7 is Critical for Capsid Assembly and
771 Envelopment. *PLoS Pathog*. 9:e1003355.

772 29. Fukuhara, T., M. Wada, S. Nakamura, C. Ono, M. Shiokawa, S. Yamamoto, T. Motomura, T.
773 Okamoto, D. Okuzaki, M. Yamamoto, I. Saito, T. Wakita, K. Koike, and Y. Matsuura. 2014.
774 Amphipathic α-Helices in Apolipoproteins Are Crucial to the Formation of Infectious Hepatitis C
775 Virus Particles. *PLoS Pathog*. 10:e1004534.

776 30. Counihan, N.A., S.M. Rawlinson, and B.D. Lindenbach. 2011. Trafficking of Hepatitis C Virus Core
777 Protein during Virus Particle Assembly. *PLoS Pathog*. 7:e1002302.

778 31. Lindenbach, B.D., and C.M. Rice. 2013. The ins and outs of hepatitis C virus entry and assembly. *Nat*
779 *Rev Microbiol*. 11:688–700.

780 32. Coller, K.E., N.S. Heaton, K.L. Berger, J.D. Cooper, J.L. Saunders, and G. Randall. 2012. Molecular
781 Determinants and Dynamics of Hepatitis C Virus Secretion. *PLoS Pathog*. 8:e1002466.

782 33. Ajjaji, D., K. Ben M'barek, B. Boson, M. Omrane, A. Gassama-Diagne, M. Blaud, F. Penin, E. Diaz,
783 B. Ducos, F.L. Cosset, and A.R. Thiam. 2022. Hepatitis C virus core protein uses triacylglycerols to
784 fold onto the endoplasmic reticulum membrane. *Traffic*. 23:63–80.

785 34. Bishé, B., G. Syed, and A. Siddiqui. 2012. Phosphoinositides in the hepatitis C virus life cycle.
786 *Viruses*. 4:2340–2358.

787 35. Berger, K.L., S.M. Kelly, T.X. Jordan, M.A. Tartell, and G. Randall. 2011. Hepatitis C Virus
788 Stimulates the Phosphatidylinositol 4-Kinase III Alpha-Dependent Phosphatidylinositol 4-Phosphate
789 Production That Is Essential for Its Replication. *J Virol*. 85:8870–8883.

790 36. Islam, K.U., S. Anwar, A.A. Patel, M.T. Mirdad, M.T. Mirdad, M.I. Azmi, T. Ahmad, Z. Fatima, and
791 J. Iqbal. 2023. Global Lipidome Profiling Revealed Multifaceted Role of Lipid Species in Hepatitis C
792 Virus Replication, Assembly, and Host Antiviral Response. *Viruses*. 15.

793 37. Hsu, N.Y., O. Ilnytska, G. Belov, M. Santiana, Y.H. Chen, P.M. Takvorian, C. Pau, H. van der Schaar,
794 N. Kaushik-Basu, T. Balla, C.E. Cameron, E. Ehrenfeld, F.J.M. van Kuppeveld, and N. Altan-Bonnet.
795 2010. Viral reorganization of the secretory pathway generates distinct organelles for RNA replication.
796 *Cell*. 141:799–811.

797 38. Prince, A., A. Tiwari, T. Mandal, D. Koiri, G. Meher, D.K. Sinha, and M. Saleem. 2024. Lipid
798 Specificity of the Fusion of Bacterial Extracellular Vesicles with the Host Membrane. *J Phys Chem B*.
799 128:8116–8130.

39. Mandal, T., N. Brandt, C. Tempra, M. Javanainen, B. Fábián, and S. Chiantia. 2025. A comparison of lipid diffusive dynamics in monolayers and bilayers in the context of interleaflet coupling. *Biochimica et Biophysica Acta (BBA) - Biomembranes*. 1867:184388.

40. Ries, J., S. Chiantia, and P. Schwille. 2009. Accurate Determination of Membrane Dynamics with Line-Scan FCS. *Biophys J*. 96:1999.

41. Petrich, A., V. Dunsing, S. Bobone, and S. Chiantia. 2021. Influenza A M2 recruits M1 to the plasma membrane: A fluorescence fluctuation microscopy study. *Biophys J*. 120:5478–5490.

42. Petrich, A., and S. Chiantia. 2023. Influenza A Virus Infection Alters Lipid Packing and Surface Electrostatic Potential of the Host Plasma Membrane. *Viruses*. 15:1830.

43. Petazzi, R.A., A.A. Koikkarah, N.D. Tischler, and S. Chiantia. 2021. Detection of Envelope Glycoprotein Assembly from Old World Hantaviruses in the Golgi Apparatus of Living Cells. *J Virol*. 95.

44. Klein, K.C., S.J. Polyak, and J.R. Lingappa. 2004. Unique Features of Hepatitis C Virus Capsid Formation Revealed by De Novo Cell-Free Assembly. *J Virol*. 78:9257–9269.

45. Shirey, C.M., J.L. Scott, and R. V. Stahelin. 2017. Notes and tips for improving quality of lipid-protein overlay assays. *Anal Biochem*. 516:9–12.

46. Davarinejad, H. Quantifications of Western Blots with ImageJ. .

47. Gandhi, S.A., S. Parveen, M. Alduhailan, R. Tripathi, N. Junedi, M. Saqallah, M.A. Sanders, P.M. Hoffmann, K. Truex, J.G. Granneman, and C. V. Kelly. 2024. Methods for making and observing model lipid droplets. *Cell Reports Methods*. 100774.

48. Chorlay, A., and A.R. Thiam. 2020. Neutral lipids regulate amphipathic helix affinity for model lipid droplets. *Journal of Cell Biology*. 219.

49. Kim, S., and J.M.J. Swanson. 2020. The Surface and Hydration Properties of Lipid Droplets. *Biophys J*. 119:1958–1969.

50. Lange, M., G. Angelidou, Z. Ni, A. Criscuolo, J. Schiller, M. Blüher, and M. Fedorova. 2021. AdipoAtlas: A reference lipidome for human white adipose tissue. *Cell Rep Med*. 2:100407.

51. Wölk, M., and M. Fedorova. 2024. The lipid droplet lipidome. *FEBS Lett*. 598:1215–1225.

52. Angelova, M.I., and D.S. Dimitrov. 1986. Liposome Electro formation. .

53. Stein, H., S. Spindler, N. Bonakdar, C. Wang, and V. Sandoghdar. 2017. Production of isolated giant unilamellar vesicles under high salt concentrations. *Front Physiol*. 8.

54. Petrich, A., V. Dunsing, S. Bobone, and S. Chiantia. 2021. Influenza A M2 recruits M1 to the plasma membrane: A fluorescence fluctuation microscopy study. *Biophys J*. 120:5478–5490.

55. Gandhi, S.A., M.A. Sanders, J.G. Granneman, and C. V. Kelly. 2023. Four-color fluorescence cross-correlation spectroscopy with one laser and one camera. *Biomed Opt Express*. 14:3812.

56. Petrášek, Z., and P. Schwille. 2008. Precise measurement of diffusion coefficients using scanning fluorescence correlation spectroscopy. *Biophys J*. 94:1437–1448.

57. Daniels, C.R., L. Kisley, H. Kim, W.H. Chen, M.V. Poongavanam, C. Reznik, K. Kourentzi, R.C. Willson, and C.F. Landes. 2012. Fluorescence correlation spectroscopy study of protein transport and dynamic interactions with clustered-charge peptide adsorbents. *Journal of Molecular Recognition*. 25:435–442.

58. Cruickshank, C. 1905. The Stokes-Einstein Law fo r Diffusion in Solution. .

59. Chenyakin, Y., D.A. Ullmann, E. Evoy, L. Renbaum-Wolff, S. Kamal, and A.K. Bertram. 2017. Diffusion coefficients of organic molecules in sucrose–water solutions and comparison with Stokes–Einstein predictions. *Atmos Chem Phys*. 17:2423–2435.

60. Perevoshchikova, I.V., D.B. Zorov, and Y.N. Antonenko. 2008. Peak intensity analysis as a method for estimation of fluorescent probe binding to artificial and natural nanoparticles: Tetramethylrhodamine uptake by isolated mitochondria. *Biochimica et Biophysica Acta (BBA) - Biomembranes*. 1778:2182–2190.

61. Turgeman, L., and D. Fixler. 2013. Time-averaged fluorescence intensity analysis in fluorescence fluctuation polarization sensitive experiments. *Biomed Opt Express*. 4:868.

62. Dunsing, V., M. Luckner, B. Zühlke, R.A. Petazzi, A. Herrmann, and S. Chiantia. 2018. Optimal fluorescent protein tags for quantifying protein oligomerization in living cells. *Sci Rep*. 8:10634.

63. Ries, J., and P. Schwille. 2012. Fluorescence correlation spectroscopy. *BioEssays*. 34:361–368.

64. Kumar, M., M.S. Mommer, and V. Sourjik. 2010. Mobility of Cytoplasmic, Membrane, and DNA-Binding Proteins in Escherichia coli. *Biophys J*. 98:552–559.

65. Chwastek, G., and P. Schwille. 2013. A monolayer assay tailored to investigate lipid-protein systems. *ChemPhysChem*. 14:1877–1881.

66. Asfia, S., R. Seemann, and J.-B. Fleury. 2023. Phospholipids diffusion on the surface of model lipid droplets. *Biochimica et Biophysica Acta (BBA) - Biomembranes*. 1865:184074.

67. Van Paridon, P.A., B. De Kruijff, R. Ouwerkerk, and K.W.A. Wirtz. 1986. BBA Report Polyphosphoinositides undergo charge neutralization in the physiological pH range: a 31P-NMR study. .

68. Merten, J.A., K.M. Schultz, and C.S. Klug. 2012. Concentration-dependent oligomerization and oligomeric arrangement of LptA. *Protein Science*. 21:211–218.

69. Borawski, J., P. Troke, X. Puyang, V. Gibaja, S. Zhao, C. Mickanin, J. Leighton-Davies, C.J. Wilson, V. Myer, I. CornellaTaracido, J. Baryza, J. Tallarico, G. Joberty, M. Bantscheff, M. Schirle, T. Bouwmeester, J.E. Mathy, K. Lin, T. Compton, M. Labow, B. Wiedmann, and L.A. Gaither. 2009. Class III Phosphatidylinositol 4-Kinase Alpha and Beta Are Novel Host Factor Regulators of Hepatitis C Virus Replication. *J Virol*. 83:10058–10074.

70. Lyn, R.K., D.C. Kennedy, A. Stolow, A. Ridsdale, and J.P. Pezacki. 2010. Dynamics of lipid droplets induced by the hepatitis C virus core protein. *Biochem Biophys Res Commun*. 399:518–524.

71. Awadh, A.A. 2023. The Role of Cytosolic Lipid Droplets in Hepatitis C Virus Replication, Assembly, and Release. *Biomed Res Int*. 2023.

72. Posor, Y., W. Jang, and V. Haucke. 2022. Phosphoinositides as membrane organizers. *Nat Rev Mol Cell Biol*. 23:797–816.

73. Lolicato, F., R. Saleppico, A. Griffo, A. Meyer, F. Scollo, B. Pokrandt, H.-M. Müller, H. Ewers, H. Hähl, J.-B. Fleury, R. Seemann, M. Hof, B. Brügger, K. Jacobs, I. Vattulainen, and W. Nickel. 2022. Cholesterol promotes clustering of PI(4,5)P2 driving unconventional secretion of FGF2. *Journal of Cell Biology*. 221.

74. Harayama, T., and H. Riezman. 2018. Understanding the diversity of membrane lipid composition. *Nat Rev Mol Cell Biol*. 19:281–296.

881 75. van Meer, G., D.R. Voelker, and G.W. Feigenson. 2008. Membrane lipids: where they are and how
882 they behave. *Nat Rev Mol Cell Biol*. 9:112–124.

883 76. Vanni, S. 2017. Intracellular Lipid Droplets: From Structure to Function. *Lipid Insights*.
884 10:117863531774551.

885 77. Vanni, S., H. Hirose, H. Barelli, B. Antonny, and R. Gautier. 2014. A sub-nanometre view of how
886 membrane curvature and composition modulate lipid packing and protein recruitment. *Nat Commun*.
887 5:4916.

888 78. Kunkel, M., and S.J. Watowich. 2004. Biophysical characterization of hepatitis C virus core protein:
889 Implications for interactions within the virus and host. *FEBS Lett*. 557:174–180.

890 79. Katen, S., and A. Zlotnick. 2009. Chapter 14 The Thermodynamics of Virus Capsid Assembly. . pp.
891 395–417.

892 80. HAGAN, M.F. 2014. Modeling Viral Capsid Assembly. . pp. 1–68.

893 81. Klein, K.C., S.R. Dellos, and J.R. Lingappa. 2005. Identification of Residues in the Hepatitis C Virus
894 Core Protein That Are Critical for Capsid Assembly in a Cell-Free System. *J Virol*. 79:6814–6826.

895 82. Mehedi, M., M. Smelkinson, J. Kabat, S. Ganesan, P. Collins, and U. Buchholz. 2017. Multicolor
896 Stimulated Emission Depletion (STED) Microscopy to Generate High-resolution Images of
897 Respiratory Syncytial Virus Particles and Infected Cells. *Bio Protoc*. 7.

898 83. Laine, R.F., A. Albecka, S. van de Linde, E.J. Rees, C.M. Crump, and C.F. Kaminski. 2015. Structural
899 analysis of herpes simplex virus by optical super-resolution imaging. *Nat Commun*. 6:5980.

900 84. Lau, L., Y.L. Lee, S.J. Sahl, T. Stearns, and W.E. Moerner. 2012. STED Microscopy with Optimized
901 Labeling Density Reveals 9-Fold Arrangement of a Centriole Protein. *Biophys J*. 102:2926–2935.

902 85. Larson, D.R., M.C. Johnson, W.W. Webb, and V.M. Vogt. 2005. Visualization of retrovirus budding
903 with correlated light and electron microscopy. *Proceedings of the National Academy of Sciences*.
904 102:15453–15458.

905 86. Duncan, A.L., T. Reddy, H. Koldsø, J. Hélie, P.W. Fowler, M. Chavent, and M.S.P. Sansom. 2017.
906 Protein crowding and lipid complexity influence the nanoscale dynamic organization of ion channels
907 in cell membranes. *Sci Rep*. 7.

908 87. Iyer, A., N.O. Petersen, M.M.A.E. Claessens, and V. Subramaniam. 2014. Amyloids of alpha-
909 synuclein affect the structure and dynamics of supported lipid bilayers. *Biophys J*. 106:2585–2594.

910 88. Auerswald, J., J. Ebenhan, C. Schwieger, A. Scrima, A. Meister, and K. Bacia. 2021. Measuring
911 protein insertion areas in lipid monolayers by fluorescence correlation spectroscopy. *Biophys J*.
912 120:1333–1342.

913